



OPEN

DATA DESCRIPTOR

Eagle-449: A volumetric, whole-brain compilation of brain atlases for vestibular functional MRI research

Jeremy L. Smith¹, Vishwadeep Ahluwalia^{2,3}, Russell K. Gore^{4,5} & Jason W. Allen^{1,4,6}✉

Human vestibular processing involves distributed networks of cortical and subcortical regions which perform sensory and multimodal integrative functions. These functional hubs are also interconnected with areas subserving cognitive, affective, and body-representative domains. Analysis of these diverse components of the vestibular and vestibular-associated networks, and synthesis of their holistic functioning, is therefore vital to our understanding of the genesis of vestibular dysfunctions and aid treatment development. Novel neuroimaging methodologies, including functional and structural connectivity analyses, have provided important contributions in this area, but often require the use of atlases which are comprised of well-defined *a priori* regions of interest. Investigating vestibular dysfunction requires a more detailed atlas that encompasses cortical, subcortical, cerebellar, and brainstem regions. The present paper represents an effort to establish a compilation of existing, peer-reviewed brain atlases which collectively afford comprehensive coverage of these regions while explicitly focusing on vestibular substrates. It is expected that this compilation will be iteratively improved with additional contributions from researchers in the field.

Background & Summary

Cortical areas responsive to vestibular stimuli were first delineated using visual and somatosensory stimuli as well as ligand-based tract-tracing in nonhuman primates. These areas include intraparietal area 2v, a section of area 3a (denoted 3aV), frontal area 6, superior parietal/supramarginal gyrus areas 7a and 7b, and a region, denoted parieto-insular vestibular cortex, or PIVC, which is located in the Sylvian fissure and is densely connected with these areas as well as the vestibular nuclei in the brainstem¹⁻⁵. Eickhoff and colleagues^{6,7} conducted histological examinations of the parietal operculum and posterior insula in humans, and proposed that the parieto-insular region was comprised of four cytoarchitectonically distinct subregions: *OP1*, the equivalent of primate secondary somatosensory cortex; *OP2*, localized to the depths of the insular-retroinsular Sylvian fissure, and for which no primate equivalent was found; *OP3*, equivalent to primate somatosensory area VS; and *OP4*, equivalent to primate area PV. In conjunction with galvanic vestibular stimulation (GVS) studies, Eickhoff *et al.* proposed that *OP2* might serve as the human homologue of the nonhuman primate PIVC. Zu Eulenberg and colleagues^{8,9} have since leveraged GVS and functional MRI (fMRI) to further localize human vestibular regions, confirming GVS-correlated responses in *OP2*, 2v, 3aV, premotor area 6, and area 7 (designated as PF in the von Economo-Koskinas system¹⁰⁻¹³), as well as the cerebellar nodules and uvula, visual area *hMST*, parietal area *PFcm*, area *hIP3* of the intraparietal sulcus, and visual cingulate (*CSv*, caudal Brodmann area 23), equivalent to primate areas VPS, VIP, and vestibular cingulate, respectively, after controlling for somatosensory, nociceptive, and salience effects, and concluded that the “core” human vestibular network likely consists of *OP2*, *hMST*, PF and *PFcm*, and *CSv*. These areas were affirmed via tractography, GVS, and resting-state functional connectivity (RSFC) based methods by Raiser *et al.*¹⁴, who also noted that the connectivity of this network is

¹Department of Radiology and Imaging Sciences, Emory University School of Medicine, Atlanta, Georgia, USA.

²Georgia Institute of Technology, Atlanta, Georgia, USA. ³GSU/GT Center for Advanced Brain Imaging, Atlanta, Georgia, USA. ⁴Wallace H. Coulter Department of Biomedical Engineering, Georgia Institute of Technology and Emory University, Atlanta, Georgia, USA. ⁵Shepherd Center, Atlanta, Georgia, USA. ⁶Department of Neurology,

Emory University School of Medicine, Atlanta, Georgia, USA. ✉e-mail: jason.w.allen@emory.edu

interhemispheric, predominantly right-lateralized, and characterized by demonstrable RSFC between homotopic regions.

More recent efforts, however, have shown that the core vestibular network is structurally¹⁵ and functionally¹⁶ interconnected with areas subserving visuospatial processing, arousal and attentional modulation (e.g., anterior insula^{17–19}), sensory gain control, proprioceptive (supramarginal gyrus, SMG^{20,21}), sensorimotor (SMG and cingulate cortex^{22,23}), cognitive-perceptual²⁴, and affective processes (SMG, subgenual cortex, and anterior insula^{25–29}). Additionally, cerebral potentials, evoked by both naturalistic and artificial vestibular stimulation, are generated not only in the parieto-insular and temporoparietal cortex of the “core” cortical vestibular system, but also in the cerebellum, frontal-prefrontal, superior parietal, and temporal cortices, as well as the posterior fossa³⁰. Vestibular function may therefore be linked with egocentric orientation and motor planning through body representation and ownership^{31,32}. Additionally, visuospatial memory, navigation, motion perception and even object-based mental image transformations have also been shown to require processing by vestibular system substrates²⁴, and all of these processes can be disrupted in cases of vestibular dysfunction. Indeed, vestibular functioning has been shown to involve the integration of multiple sensory modalities³³, and syndromes such as persistent postural-perceptual dizziness (PPPD) and post-concussive vestibular dysfunction (PCVD) have been associated with maladaptive visual and visuospatial processing^{34–37}. Furthermore, vestibular manipulation elicits affective responses^{38,39} and vestibular dysfunction may induce or exacerbate anxiety, depression, and other affective conditions^{33,40} or, conversely, can be modulated by affective conditions such as state and trait anxiety⁴¹. Neuroimaging research which incorporates not only cortical areas but also structures in the basal ganglia, thalamus, and posterior fossa would therefore contribute considerably to vestibular systems neuroscience and patient care. Large neuroimaging consortia comprised of datasets from both normative adults and adolescents, including the Human Connectome Project⁴², UK Biobank⁴³, and Adolescent Brain Cognitive Development studies⁴⁴, as well as those with mild traumatic brain injury, such as the Long-Term Impact of Military-Relevant Brain Injury Consortium-Chronic Effects of Neurotrauma Consortium, or LIMBIC-CENC, effort^{45–47}, are available for comprehensive exploration and hypothesis testing. To date, however, no neuroimaging atlas offers the extensive coverage necessary for researchers to explore vestibular system-associated connectivity across the cortex, subcortical structures, cerebellum, and brainstem. With source validation, such coverage would also afford validation of fMRI-based vestibular research using electroencephalography (EEG) and functional near-infrared spectroscopy (fNIRS), which, while limited in spatial resolution relative to fMRI and generally constrained to cortical areas, do allow naturalistic head movements in experimental contexts⁴⁸.

The present paper attempts to address this omission by provisioning a compilation of volumetric brain atlases in MNI stereotactic space which, in composite, comprises the entirety of the brain. It is hoped that further development and refinement of this compilation will be supported by the neuroimaging community; recent research, for example, indicates that the OP2 region may consist of functional⁴⁹ and structural¹⁵ subdivisions, such as the posterior insular complex, which exhibit distinct connectivity patterns, and these subdivisions may need to be included in future versions of the compilation. Thus, the present version (denoted Eagle-449 to indicate that it includes 449 regions of interest) represents an initial effort toward providing an important resource for research into vestibular function and dysfunction and the expanding list of regions functionally associated with the vestibular system.

Methods

Generation of the vestibular atlas. Six parcellations were leveraged for this compilation, including the Eickhoff Anatomy atlas, which is a primary component of the JuBrain/SPM Anatomy Toolbox (<https://github.com/inm7/jubrain-anatomy-toolbox>)^{50–52}; the SUIT anatomical cerebellar parcellation by Diedrichsen *et al.* (https://github.com/DiedrichsenLab/cerebellar_atlases/tree/master/Diedrichsen_2009)⁵³; anatomical parcellations of the thalamus⁵⁴ and hypothalamus⁵⁵ by Najdenovska *et al.*⁵⁶ and Neudorfer *et al.*⁵⁷ respectively; and divisions of the brainstem and diencephalon provided as part of the Brainstem Navigator template^{58–64}. All cortical areas not included in the Eickhoff parcellation were obtained from the Brainnetome atlas (<https://atlas.brainnetome.org>) by Fan *et al.*^{65–69}. All atlases were resampled to MNI152 stereotactic space, if necessary, registered to the 1 mm isometric MNI152 T1 template (version 2009c) using 3-dof linear registration, inspected and corrected for overlapping voxels, and masked against the MNI152 white matter and cerebrospinal fluid templates. “Orphan” voxels, defined as very small voxel clusters which were not contiguous with a larger cluster in-plane or within adjacent slices, were then removed using the AFNI program 3dmerge⁷⁰, which performed voxel clustering using a maximum inter-voxel connection radius of 1.7 mm. Finally, “liminal” voxels, defined as contiguous but thin edges of 1–4 voxel thickness, and which were usually the result of remnant ROI edges, often in occipital cortex, following subtraction of other atlases from the Brainnetome parcellation, were manually removed by editing in AFNI (Fig. 1).

Several ROIs identified as “vestibular” by Eickhoff^{6,7}, zu Eulenberg^{8,9}, and others^{14,15,71,72}, including OP2/PIVC+, the posterior insular complex (PIC), visual cingulate (CSv), somatosensory areas 2v and 3aV, premotor area 6, and inferior parietal areas IPS3, PF, and PFcm, as well as cortical and subcortical structures subserving “multimodal vestibular” or “extended vestibular” areas which are responsive to vestibular stimulation but perform non-vestibular-specific functions, such as spatial localization and recall, visuo-vestibular processing, integration of somatosensory and motor information, and representation of peri-personal space, including the medial temporal lobe, insula, precuneus, and temporal lobe^{15,16}, were well-represented in the Eickhoff-Indovina or Brainnetome parcellations. These are presented in Table 1.

Additional preprocessing details for each parcellation are provided below. For a comprehensive list of all ROIs obtained from each atlas, as well as atlas labels, ROI values, and ROI size, refer to **Supplementary Tables – Atlas Labels**. All preprocessed parcellations, ROI label files (also known as lookup tables or LUTs), and preprocessing

SOURCES

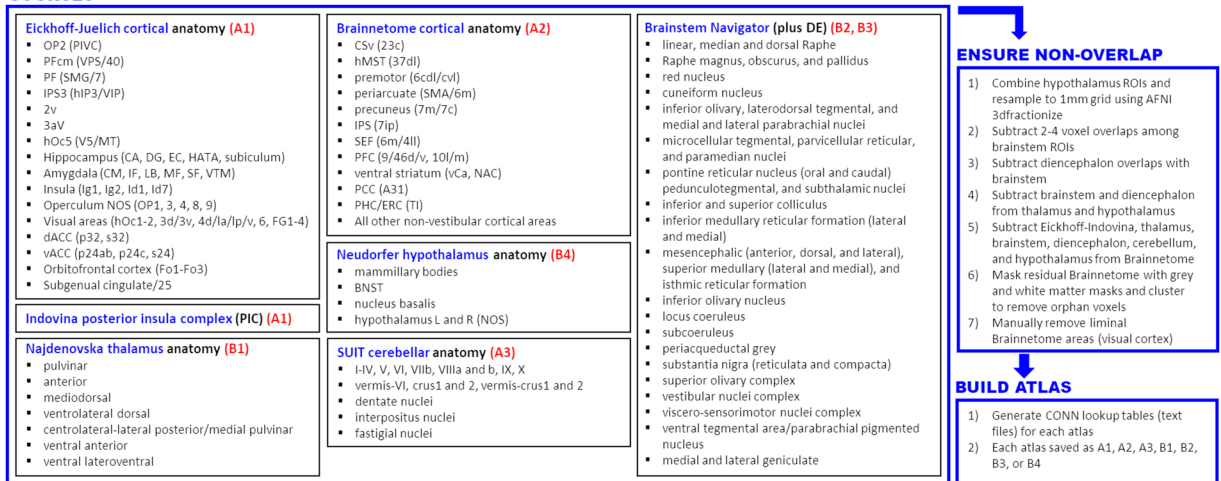


Fig. 1 Depiction of the compiled atlas-generation process from source atlas data. Sources (largest panel) included the Eickhoff-Juelich cortical parcellation in addition to left- and right-hemisphere posterior insular complex (PIC) regions of interest (ROIs) provided by Indovina *et al.*, which were incorporated into atlas A1; the Diedrichsen-SUIT anatomical cerebellum parcellation, incorporated into atlas A3; an anatomical thalamus parcellation by Najdenovska *et al.*, incorporated into atlas B1; an anatomical hypothalamus parcellation by Neudorfer *et al.*, incorporated into atlas B4; and brainstem and diencephalon ROIs provided as part of the Brainstem Navigator atlas and incorporated as atlases B2 and B3, respectively (see text for source references). Cortical areas not included in atlas A1 were incorporated from the Fan Brainnetome atlas as atlas A2. In all cases, source ROIs were aligned to the 1 mm isometric MNI152 T1 template and adjusted for overlaps, as detailed in the text; additionally, some hypothalamic ROIs were merged and downsampled from the source 0.5 mm isometric to final 1 mm isometric grid. All T1-registered source ROIs were masked against cerebrospinal fluid and white matter templates, and isolated voxel clusters were edited manually and via clustering (*Ensure non-overlap* panel). Finally, lookup tables were generated for each of the final seven atlases for import into the CONN Toolbox (*Build atlas* panel).

code have been made available on the Neuroimaging Informatics Tools and Resources Collaboratory Resources Registry (NITRC repository)⁷³. The compiled atlas is presented as Fig. 2.

Cortical parcellation. *Eickhoff-Juelich anatomical cortical parcellation (Atlas A1).* The Eickhoff-Juelich (JuBrain) cytoarchitectonic parcellation is comprised of several known vestibular ROIs, including divisions of the parietal operculum, such as OP2 and secondary somatosensory cortex^{6,7,74}, primary somatosensory cortex, including area 3a^{75,76}, visual area MT/V5⁷⁷, superior parietal cortex, including area 7^{78,79}, and inferior parietal cortex, including areas PF and PFcm^{80,81}. A number of ROIs encompassing the hippocampus⁸², insula⁸³, amygdala⁸², cingulum⁸⁴, orbitofrontal cortex⁸⁵, and visual areas^{86–90} were also included from this parcellation. 102 JuBrain atlas ROIs, along with left- and right-hemisphere posterior insular complex (PIC), derived from the disjunction of the Brainnetome atlas BA40rv and Eickhoff atlas OP2 ROIs and provided by Indovina *et al.*¹⁵, were incorporated as *Atlas A1*. To create Atlas A1, the left (L) and right (R) PIC ROIs, as well as SUIT cerebellar (Atlas A3), thalamic (Atlas B1), and brainstem and diencephalon ROIs (atlases B2 and B3) were subtracted from other JuBrain atlas regions.

Brainnetome structural-functional cortical parcellation (Atlas A2). The JuBrain parcellation does not comprise the entire cerebral cortex, and some areas commonly associated with vestibular processing, including hMST and visual cingulate (caudal Brodmann area 23), are not well-defined. Consequently, all cortical ROIs not defined in Atlas A1 were generated from the Brainnetome atlas, which is premised on the functional and structural connectivity of cortical regions, as *Atlas A2*. To avoid overlaps with other parcellations, a binary mask comprised of atlases A1, A3 (cerebellar), B1 (thalamic), B2 (brainstem), and B3 (diencephalon) was subtracted from the Brainnetome parcellation. As a result of this subtraction, some ROIs conventionally included in the Brainnetome parcellation, including occipitopolar cortex (OPC), medioventral (cLinG) and lateral occipital cortex (iOccG), L lateral amygdala (lAmygL), and R entorhinal area 28/34 (A28/34), contain zero voxels in the final Atlas A2. However, these regions are indexed in the LUTs for comprehensiveness, for a total 229 Atlas A2 ROIs.

The Brainnetome parcellation does not contain cerebellar ROIs, but does define several ROIs from subcortical structures, including cingulate, caudate, putamen, globus pallidus, and nucleus accumbens, and these structures are also included in Atlas A2. Additionally, some larger cortical areas, such as superior parietal area hIPS3 and postcentral area 2, are more restrictively defined in the JuBrain/A1 atlas, and portions of these areas which are contiguous with, but do not overlap with, A1 areas are also included in Atlas A2. Finally, Atlas A2 contains liminal remnants of other cortical regions which were not defined as part of other atlases, but were too large and

	ROI	ROI Label	Atlas	ROI ID	Voxels
Vestibular	L posterior insular complex	PIC L	A1	1	1713
	R posterior insular complex	PIC R	A1	2	1844
	L inferior parietal/supramarginal area PFcm	IPL PFcm L	A1	25	2984
	R inferior parietal/supramarginal area PFcm	IPL PFcm R	A1	75	1841
	L inferior parietal area PF/40/anterior supramarginal gyrus	IPL PF L	A1	26	4537
	R inferior parietal area PF/40/anterior supramarginal gyrus	IPL PF R	A1	76	6161
	L parietal area OP2 (parieto-insular vestibular cortex, PIVC)	OP2 L	A1	31	519
	R parietal area OP2 (parieto-insular vestibular cortex, PIVC)	OP2 R	A1	81	812
	L dorsolateral middle temporal area 37/hMST	A37dl L	A2	85	4660
	R dorsolateral middle temporal area 37/hMST	A37dl R	A2	86	5594
	L vestibular nuclei complex	VestibN L	B2	61	201
	R vestibular nuclei complex	VestibN R	B2	62	188
	L caudal cingulate area 23 (cingulate sulcus visual, CSv)	A23c L	A2	185	4731
	R caudal cingulate area 23 (cingulate sulcus visual, CSv)	A23c R	A2	186	4401
Extd. vestibular	L hIPS3/hIP3/VIP	AIPS IP3 L	A1	3	3606
	R hIPS3/hIP3/VIP	AIPS IP3 R	A1	53	3842
	L primary somatosensory area 2	PSC 2 L	A1	36	5186
	R primary somatosensory area 2	PSC 2 R	A1	86	5563
	L primary somatosensory area 3a	PSC 3a L	A1	37	2135
	R primary somatosensory area 3a	PSC 3a R	A1	87	1457
	L visual area V5/MT	Vis hOc5 L	A1	51	674
	R visual area V5/MT	Vis hOc5 R	A1	101	710
	L intraparietal/superior parietal area 7 (hIP3) (Brainnetome)	A7ip L	A2	133	2482
	R intraparietal/superior parietal area 7 (hIP3) (Brainnetome)	A7ip R	A2	134	2371
	L postcentral area 2 (Brainnetome)	A2 L	A2	159	1259
	R postcentral area 2 (Brainnetome)	A2 R	A2	160	2961

Table 1. Regions of interest (ROIs) identified as “vestibular” or “extended vestibular” (*Extd. vestibular*) atlas number (*ROI ID*), label and label numbers within the atlas, and number of voxels within the ROI. Abbreviations: *L*, left hemisphere; *R*, right hemisphere.

contiguous to be considered “orphan” voxel clusters. These remnants are typically found in the occipital lobe in the vicinity of the parieto-occipital sulcus.

Cerebellar parcellation. *Diedrichsen-SUIT anatomical parcellation (Atlas A3).* The SUIT cerebellar atlas is premised on anatomical delineations of cerebellar structures and is provided as part of the SUIT Toolbox. It was incorporated into this compilation, without modification, as *Atlas A3*, and is comprised of 34 ROIs. ROIs included in the SUIT parcellation were subtracted from other atlases, as noted elsewhere in this section.

Subcortical and brainstem structures. *Najdenovska anatomical thalamus parcellation (Atlas B1).* Many atlases include a delineation of the thalamus which is based on the functional connectivity analyses by Behrens *et al.*^{91,92}. Our present atlas compilation, however, is primarily based on anatomical delineation of cerebral structures, and, for consistency, we opted to include the thalamic parcellation by Najdenovska *et al.*⁵⁶ as *Atlas B1*, comprised of 14 ROIs. Brainstem and diencephalon ROIs (atlases B2 and B3) overlapped with the edges of some of these thalamic areas by approximately 1–3 voxels, and were subtracted from *Atlas B1* accordingly. A mask comprised of ROIs from *Atlas B1* was also subtracted from atlases A1 and A2, as previously noted, as well as from *Atlas B4* (hypothalamus). Lateral and medial geniculate nuclei (LGN, MGN) were included with diencephalic regions (*Atlas B3*).

Brainstem Navigator (brainstem and diencephalon: Atlases B2 and B3). Brainstem and diencephalon ROIs were incorporated into this atlas compilation as Atlases B2 and B3, respectively. Some minor overlaps of 1–2 voxels were noted among these ROIs; accordingly, each pair of ROIs was assessed for voxel overlap, and overlapping voxels were retained from the smaller, and subtracted from the larger, of the pair. A mask of the *Atlas B2* and *B3* ROIs was created following this procedure and subtracted from atlases A1 and B1, as previously noted, as well as from *Atlas B4* (hypothalamus). The final B2 atlas was comprised of 66 ROIs, and the B3 atlas of 6 ROIs, including L and R LGN and MGN and L and R subthalamic nuclei. Notably, the vestibular nuclei complex, an important component of the vestibular system, is included in *Atlas B2* (Table 1).

Neudorfer anatomical hypothalamus parcellation (Atlas B4). The detailed hypothalamic parcellation by Neudorfer and colleagues⁵⁷ is originally defined in 0.5 mm isometric space and required additional processing for inclusion in the 1 mm compilation. As part of this process, larger ROIs, such as the L and R mamillary bodies,

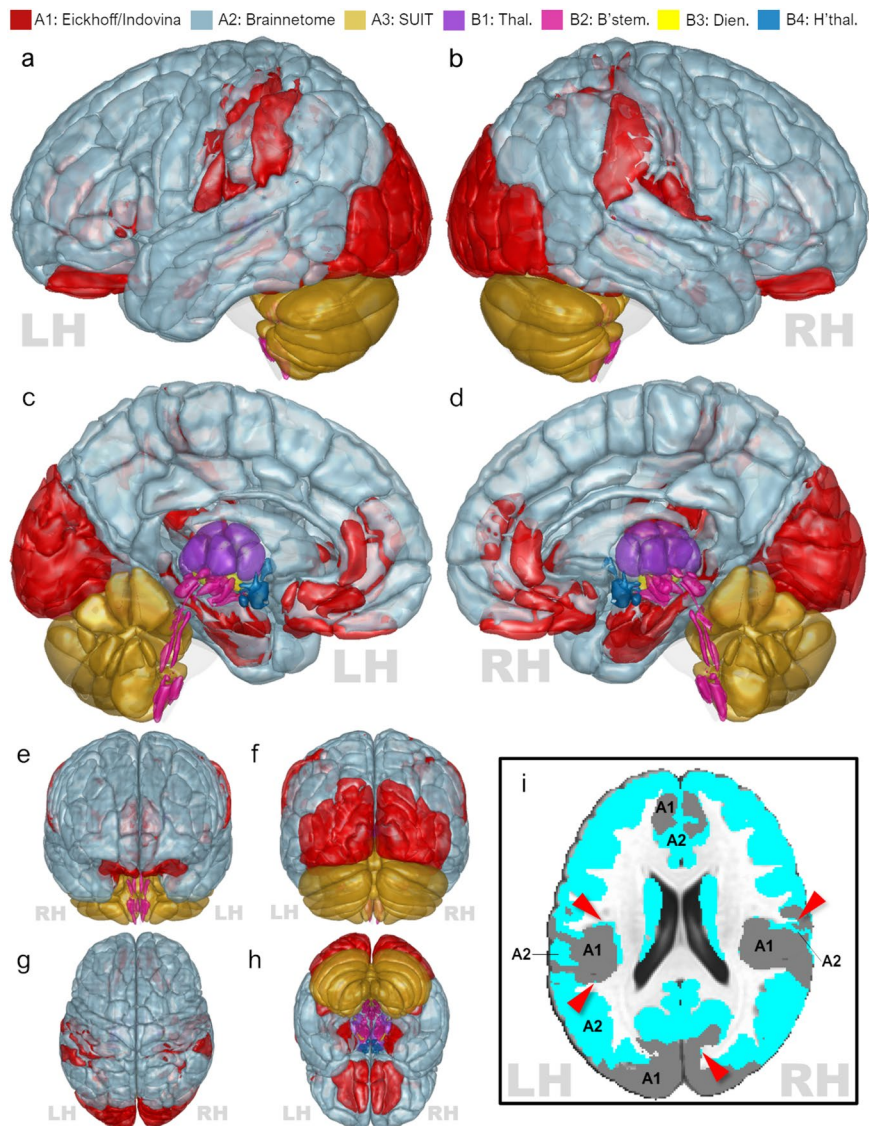


Fig. 2 Rendering of the composite atlas. Regions of interest (ROIs) from each of the seven constitutive atlases are overlaid on the 1 mm isometric MNI152 T1 template and rendered at 50% opacity. Note that ROI extents are approximate due to the necessity of vertex smoothing operations for rendering. (**a**) Left view; (**b**) right view; (**c**) left medial view; (**d**) right medial view; (**e**) anterior view; (**f**) posterior view; (**g**) superior view; (**h**) inferior view. Inset (**i**) depicts a representative axial section ($z = +21$ mm) demonstrating that some Brainnetome ROIs (atlas A2, blue) are remnants of anatomically-defined areas which are generally, but not entirely, included in the Eickhoff/Indovina-derived atlas (atlas A1, grey). These ROIs are often liminal to, or interdigitated with, the larger atlas A1 ROIs (red arrows). There is, therefore, some overlap in ROI names between the two atlases, and users are discouraged from leveraging atlas A2 without inclusion of atlas A1. LH and RH indicate left and right hemisphere, respectively. Abbreviations: *Thal.*, adapted from anatomical thalamus parcellation by Najdenovska *et al.*; *B'stem*, *Dien.*, brainstem and diencephalon ROIs adapted from Brainstem Navigator; *H'thal.*, adapted from anatomical hypothalamus parcellation by Neudorfer *et al.*

bed nuclei of the stria terminali, and L and R nucleus basalis were retained; however, the final 1 mm resolution, relative to the size of several other nuclei of interest, including the medial preoptic, paraventricular, periventricular, dorsal paraventricular, ventromedial, dorsomedial, supraoptic, suprachiasmatic, tuberomammillary, and arcuate nuclei, as well as the lateral, anterior, and posterior hypothalamus, necessitated their merger into L and R “hypothalamus, not otherwise specified (NOS)” ROIs. Downsampling to the 1 mm isometric grid was performed with the AFNI program 3dfractionize; various 3dfractionize clipping levels (percent voxel occupation) from 0.1 (10%) to 0.8 (80%) were assessed, and a clipping level of 40% ultimately selected, as this yielded ROI borders which most closely matched those in the original, 0.5 mm isometric grid. Minor overlaps between the Neudorfer hypothalamus, Brainstem Navigator, and Najdenovska thalamus ROIs were resolved by subtraction of binary masks representing atlases B1, B2, and B3 from the downsampled ROIs. Eight ROIs remained after this subtraction and are included in the compilation as *Atlas B4*. A partial view of the original Neudorfer *et al.* and final

	22–25 yrs	26–30 yrs	31–35 yrs	≥36 yrs	Total
Female	69	187	155	8	419
Male	124	179	97	2	402
Total	193	366	252	10	821

Table 2. Age and sex of Human Connectome Project (HCP) participants leveraged for the present study.

Atlas B4 ROIs, following downsampling and subtraction of brainstem and diencephalon ROIs (Atlas B2 and B3), is provided as Supplementary Figure 2.

Data Records

The Eagle-449 atlas compilation has been made available on NITRC⁷³, under an open/attribution license, in the form of Gzipped, NIfTI-format volumetric datasets for atlases a1-a3 and b1-b4; text-format lookup tables (LUTs) for each atlas based on assigned ROI value; a spreadsheet containing ROI values, abbreviations, full labels, ROI group (e.g., *somatomotor*, *orbitofrontal*, *cerebellum*); and suggested ROI labels and ROI ordering for use with the CONN Toolbox⁷³. The present version, v449, resides in the *EAGLE449* folder on the associated GitHub repository, and it is expected that future iterations of the atlas compilation, which will be based on additional contributions from vestibular neuroimaging researchers, will be placed in separate subfolders in the same repository.

Technical Validation

Participants and MRI acquisitions. The present study evaluated rsfMRI data from a total 821 datasets from young, healthy adult subjects (402 male, 419 female) included in the HCP S500 (n = 269), S900 (n = 350), and S1200 (n = 202) public data releases. Additional information on HCP inclusion and exclusion criteria may be found in Van Essen⁴². One rsfMRI acquisition, acquired using a Siemens Skyra 3 T MRI (1200 frames at TR = 720msec, 72 slices, TE = 33.1msec, FA = 52°, 2 mm isometric voxels, 208 × 180 mm FOV)⁹³, previously denoised by the HCP using the FIX denoising pipeline and normalized to the standard MNI152 brain template (REST1_LR_hp2000_clean), as well as a preprocessed T1-weighted anatomical image, was obtained for each participant. The FIX pipeline includes application of a highpass filter at 2000 sec, motion regression, and regression of noise components identified via independent components analysis⁹⁴. Only data preprocessed with the most recent HCP preprocessing workflow, version r227, were included. Subject ages ranged from 22 to 36 years (see Table 2).

Data preprocessing. Given the denoising and normalization already applied to the subject T1 and resting state data as part of the FIX-denoising process, the current workflow, performed in the CONN Toolbox version 21b, was limited to minimal preprocessing standards and consisted of tissue segmentation to obtain mean white matter and CSF signal, minimal correction or residual subject motion and identification of framewise outliers, ordinary least-squares regression of white matter, CSF, and motion noise sources, and smoothing of residual data using a 4 mm FWHM Gaussian kernel as well as an 8–250 mHz bandpass. Quality assurance results are provided as Supplementary Figure 1 – **Quality Control**.

Functional connectivity analysis. To test the atlas compilation, semipartial correlations were computed, using the CONN Toolbox, between the right (R) OP2, R PIC, and all 447 remaining ROIs from the seven component parcellations. The semipartial correlation coefficient, or SPCC, between ROI pairs controls for other ROIs' mediating effects on those pairs, and thus represents an estimate of the “direct” or “effective” connectivity between them^{95–97}. For this analysis, the Fisher-transformed SPCC, $Z(i, j)$, was computed for each pair of ROIs using the ROI timeseries $R_i(t)$ and the matrix β of multivariate regression coefficients:

$$R_j(t) = \sum_{i \neq j} \beta(i, j) R_i(t) + \epsilon_j(t)$$

where $\beta(i, j)$ is estimated by ordinary least squares:

$$\beta(i, j) | \min_{\beta(i, j)} \int \epsilon^2(t) dt,$$

and the normalized SPCC,

$$Z(i, j) = \tanh^{-1}(\beta(i, j) \sqrt{c}),$$

Is computed as

$$c = \frac{\int \tilde{R}^2(t) dt}{\int R_j^2(t) dt}$$

The matrix \mathbf{Z} of all SPCCs was then subjected to a one-sample t -test and a “threshold-free cluster enhancement” (TFCE) score⁹⁸ computed for each connection and for groups of neighboring connections

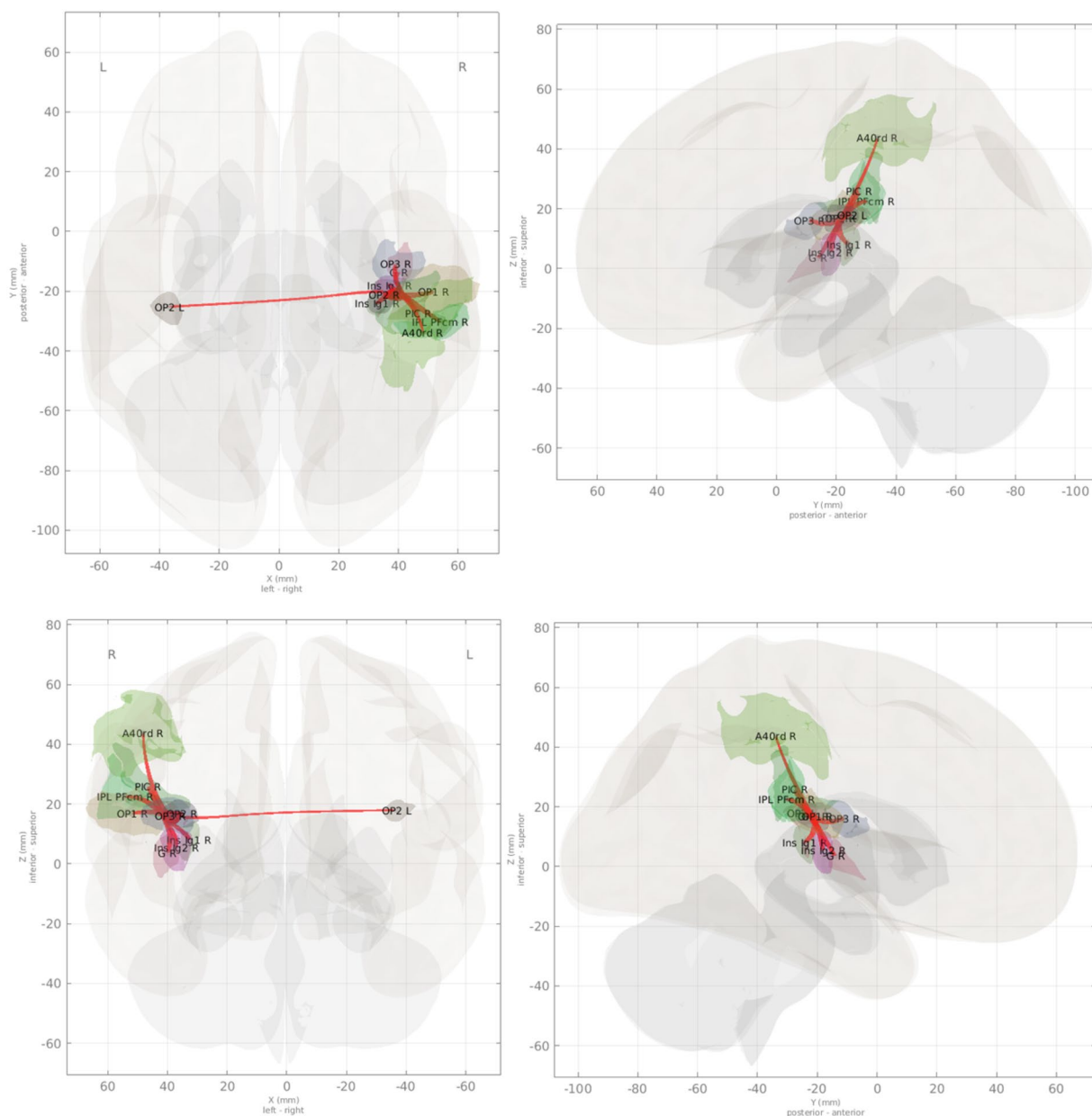


Fig. 3 Connections of right-hemisphere parieto-insular region OP2, derived from semi-partial correlations with the R OP2 seed voxel signal after preprocessing and denoising. Connections in this figure are adjusted for multiple comparisons correction using threshold-free cluster enhancement (TFCE) with a familywise error rate $p \leq 0.05$ (see *Technical Validation – Functional connectivity analysis* section of the text). Compare with Indovina *et al.*¹⁵.

(subgraphs or “clusters”) from the resulting matrix of t -statistics. Hypothesis testing proceeded by comparing the t -value for each connection with an estimate of a TFCE “extent” parameter at various thresholds and comparing the results with an expected null distribution of TFCE values estimated using 1000 permutations of the original data. This procedure yielded a “peak-level” familywise error rate (FWE)-corrected p-value, representing the likelihood of detecting one or more connections with the observed TFCE value or larger over all connections in Z. “Peak-level” uncorrected and false discovery rate (FDR)-corrected p-values were also estimated for each local extremum in the TFCE score matrix, representing the likelihood of observing its TFCE score, or larger, in at least one other randomly-selected extremum in the TFCE score matrix, or the expected proportion of false discoveries for that extremum’s TFCE score or greater.^{97,99} For hypothesis testing, the current TFCE results were corrected for multiple comparisons at $p(\text{FWE}) \leq 0.05$.

The CONN Toolbox computes TFCE using an exact integration method. Note that the definition of a “cluster” of connections for TFCE is partly dependent on ROI sorting, and this sorting algorithm may be implemented manually or through hierarchical clustering based on anatomical proximity or functional similarity¹⁰⁰. For the present (exploratory) purposes, ROIs were sorted by anatomical or functional domain, including

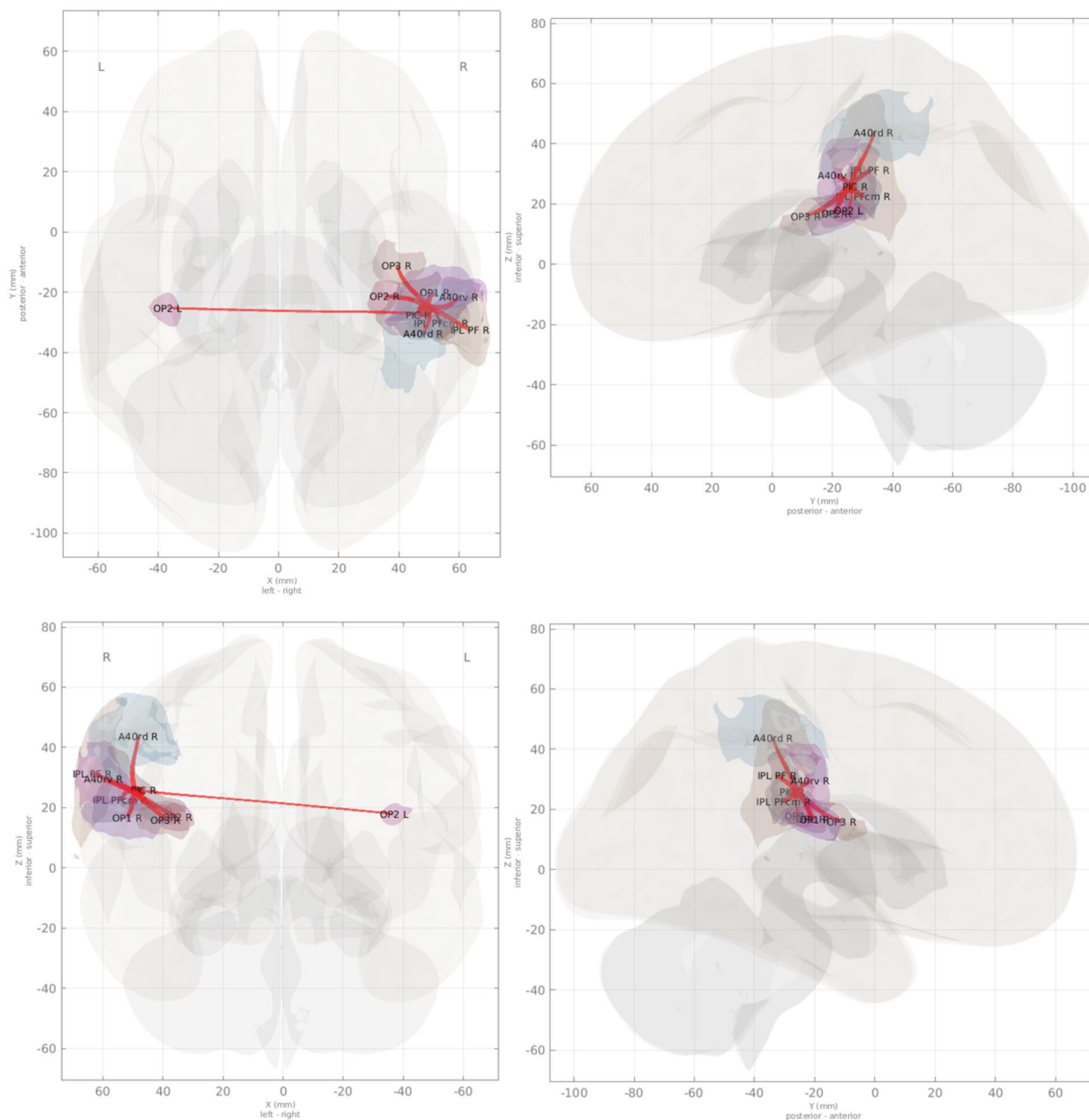


Fig. 4 Connections of right-hemisphere parieto-insular region PIC, derived from semi-partial correlations with the R PIC seed voxel signal after preprocessing and denoising. Connections in this figure are adjusted for multiple comparisons correction using threshold-free cluster enhancement (TFCE) with a familywise error rate $p \leq 0.05$ (see *Technical Validation – Functional connectivity analysis* section of the text). Compare with Indovina *et al.*¹⁵.

vestibular or extended vestibular based on prior publications^{14,15}, or orbitofrontal-prefrontal, frontal, somatomotor, somatosensory, visual, superior or inferior parietal, superior or middle-temporal, medial temporal, insular, and cingulate. FWE, FDR, and uncorrected p-values for connection clusters and individual connections did not differ substantially between this manual sorting and the default CONN hierarchical algorithm; other algorithms may, however, be preferable¹⁰¹.

Results. Semipartial correlations, corrected for multiple comparisons using TFCE, are shown for the R OP2 and R PIC seed ROIs in Fig. 3, 4, respectively, and results provided for first-order connections to these ROIs are presented in Table 3. R OP2 connections in this normative cohort included R parietal area PFcm, OP1, OP3, insular areas G, Ig1, and Ig2, PIC, and rostradorsal area 40 (40rd/area PFt), as well as L OP2. Connections with R PIC included R PFcm, PF, OP1, OP3, OP2, rostroventral area 40 (area PFop), and rostradorsal area 40/PFt, as well as L OP2. Note that, although TFCEs for the R OP2:R PFcm, R OP2:R 40rd/PFt, R PIC:40rd/PFt, and R PIC-L OP2 parent clusters were statistically significant at $p(FWE) \leq 0.05$ and $p(FDR) \leq 0.05$, these associations did not survive multiple comparisons correction at the connection level. These results compare favorably with the structural

R OP2	R PIC	Connection	t(820)	p(FDR)	p(FWE)
		Cluster 75/690: TFCE 3174.31, p(unc) <0.0001, p(FDR) <0.0001, p(FWE) <0.0001			
	■	[EI] PIC R: [EI] IPL PFcm R	21.55	<0.0001	<0.0001
	■	[EI] PIC R: [EI] IPL PF R	6.55	<0.0001	<0.0001
■		[EI] OP2 R: [EI] IPL PFcm R	1.79	0.0741	0.5974
		Cluster 164/690: TFCE 1136.96, p(unc) <0.0001, p(FDR) <0.0001, p(FWE) <0.0001			
	■	[EI] PIC R: [EI] OP1 R	15.16	<0.0001	<0.0001
■		[EI] OP2 R: [EI] OP1 R	6.77	<0.0001	<0.0001
		Cluster 446/690: TFCE 118.4, p(unc) <0.0001, p(FDR) <0.0001, p(FWE) <0.0001			
■		[EI] OP2 R: [EI] OP3 R	7.28	<0.0001	<0.0001
	■	[EI] PIC R: [EI] OP3 R	3.64	0.0003	0.0133
		Cluster 475/690: TFCE 98.7, p(unc) <0.0001, p(FDR) <0.0001, p(FWE) <0.0001			
■		[EI] OP2 R: [EI] Ins Ig1 R	6.59	<0.0001	<0.0001
		Cluster 504/690: TFCE 81.67, p(unc) <0.0001, p(FDR) <0.0001, p(FWE) <0.0001			
■		[EI] OP2 L: [EI] OP2 R	5.42	<0.0001	<0.0001
	■	[EI] OP2 L: [EI] PIC R	2.51	0.0122	0.2552
		Cluster 571/690: TFCE 55.68, p(unc) <0.0001, p(FDR) <0.0001, p(FWE) <0.0001			
■		[EI] OP2 R: [EI] Ins Ig2 R	4.65	<0.0001	0.0002
		Cluster 583/690: TFCE 53, p(unc) <0.0001, p(FDR) <0.0001, p(FWE) = 0.001			
■	■	[EI] OP2 R: [EI] PIC R	4.3	<0.0001	0.0011
		Cluster 607/690: TFCE 48.52, p(unc) <0.0001, p(FDR) <0.0001, p(FWE) = 0.002			
■		[EI] OP2 R: [BN] G R	5.35	<0.0001	<0.0001
		Cluster 650/690: TFCE 42.67, p(unc) <0.0001, p(FDR) <0.0001, p(FWE) = 0.01			
	■	[EI] PIC R: [BN] A40rv R	5.15	<0.0001	<0.0001
■		[EI] OP2 R: [BN] A40rd R	1.63	0.1041	0.6648
	■	[EI] PIC R: [BN] A40rd R	0.78	0.4353	0.9016

Table 3. First-order connections of right (R) OP2 and R PIC derived from semipartial correlations across all 449 pairs of ROIs in the composite atlas and corrected for multiple comparisons using TFCE. ROI abbreviations are listed in Supplementary Table 1. A report containing statistics for connections of all vestibular areas (as listed in Table 1) is provided as Supplementary Table 2. Other abbreviations: *FDR*, false discovery rate correction; *FWE*, familywise error rate correction; *unc*, uncorrected.

findings of Indovina *et al.*¹⁵ except that no connection between R PIC and L motor area 4a was observed in the current results, but were reported by Indovina *et al.*, and a connection between R OP2 and ipsilateral PFT was observed in the current results, but was not reported by Indovina *et al.* Additionally, a suprathreshold number of streamlines originating from, or terminating in, R OP2 or R PIC, were observed in the latter study which were not supported, in terms of functional connectivity, here. Neither R OP2 nor R PIC exhibited connectivity with thalamic, brainstem, or cerebellar nuclei. In both cases, however, connectivity was predominantly localized to the right hemisphere, and characterized by homotopic connections with the seed ROIs. All semipartial correlations were positive, indicating in-phase relationships between the seed and target ROIs.

Statistics for all extant connections following TFCE correction are also provided as Supplementary Table 2. Several interesting connections were observed between conventional vestibular regions and areas not typically included in the “core” vestibular network, including R somatosensory area 2 and ipsilateral rostral hippocampus (connection $t = +2.3800$, $p(FDR) = 0.0176$, but $p(FWE) = 0.3157$), R area 7ip and ipsilateral laterobasal amygdala (connection $t = +1.8700$, but $p(FDR) = 0.0623$ and $p(FWE) = 0.5625$), and extensive interconnectivity between cortical vestibular areas 37 dl/hMST and 7ip and visual areas FG2, FG4, lateral-anterior and lateral-posterior area hOc4, and between hOc5, postcentral area 2, and regions of the cerebellum, including L crus, R V, VI, VIIb, and VIIIa. Additionally, several cortical and subcortical vestibular areas, including area PF and the vestibular nucleus complex, were functionally connected with subcortical and brainstem nuclei, such as the subcoeruleus, laterodorsal tegmental nucleus, medial parabrachial nucleus, globus pallidus, and caudal-dorsal cingulate area 24.

Limitations of the validation process. The current version, v449, of the atlas compilation, as well as its technical validation, incurs several caveats. With respect to the compilation itself, it is important to note that the Brainnetome parcellation (Atlas A2) serves as a “catch-all” for cortical areas not included in Atlas A1, and, as previously noted, includes liminal remnants of Atlas A1 ROIs. Consequently, Atlas A2 should not be used independently of Atlas A1, and future versions of the atlas compilation may substitute other anatomically-derived cortical parcellations for, or in addition to, the Brainnetome source. Investigators are also encouraged to consider whether the Brainnetome parcellation comports with their research aims, as some cortical parcellations, including functionally-defined parcellations such as that of Gordon *et al.*¹⁰² may be more suitable for specific purposes. Additionally, based on recent analyses which have delineated functional subdivisions within vestibular areas,

including OP2, it appears likely that these areas, as currently defined, are composites of subregions which subserve differential vestibular functions⁴⁹.

“Validation” of the current atlas compilation was conducted by computing semi-partial correlation coefficients between right-hemisphere OP2 and PIC seeds and all other ROIs, and comparing the results to previous peer-reviewed findings concerning the connectivity of these regions^{14,15}. While these qualitative comparisons were favorable in that they replicated prior results, it should be noted that there are numerous ways, in addition to semi-partial correlation, to assess RSFC. Analyses which leveraged “classical” Pearson correlations failed to resolve network structures, such as connections between vestibular nuclei and other areas, which would be expected based on prior anatomical and structural findings in humans and lower primates, and the technical validation process therefore leveraged semi-partial correlations in order to control for the influence of all other connections with the seed and target ROIs. Due to the nature of semi-partial correlation, however, removing one or more of these regions may effect a new network topology. Finally, the topologies resolved in this validation process are likely incomplete, due not only to inherent issues of multiple comparisons (which were addressed to some degree by the use of TFCE), but potentially due to suppressed effect sizes in the connectivity of the subcortical regions of HCP datasets due to MRI acquisition parameters, which have been noted as problematic by Risk and colleagues^{102,103}.

Usage Notes

The entirety of the dataset may be downloaded from GitHub (<https://github.com/EmoryPcvdLab/EagleVAC>) or NITRC⁷³. The current version, v449, resides in the EAGLE449 folder of the GitHub repository. As the present authors did not have a role in the acquisition, processing, or distribution of the source atlases, investigators who leverage the atlas are requested to cite these original sources as described in the README file of the repository. It is also requested that investigators consider contributing to iterative refinements of the EAGLE atlas compilation, including, but not limited to, correction of errors, modifications to ROIs, and newly-derived subdivisions of existing vestibular areas documented in published, peer-reviewed research. Finally, investigators should be aware of the number of simultaneous tests (number of ROIs) relative to their sample size when leveraging these parcellations.

Code availability

The BASH shell script used for merging of source atlases has also been made available on the GitHub repository as *merge_code.bash*. Investigators who wish to replicate the workflow will need to download the original source atlases and adjust file paths in the shell script to point to them. The script requires a recent version of the AFNI suite⁷⁰.

Received: 17 August 2022; Accepted: 4 January 2023;

Published online: 14 January 2023

References

- Akbarian, S. *et al.* Responses of single neurons in the parietoinsular vestibular cortex of primates. *Ann N Y Acad Sci* **545**(1), 187–202, <https://doi.org/10.1111/j.1749-6632.1988.tb19564.x> (1988).
- Brandt, T. Vestibular cortex: its locations, functions, and disorders. *Vertigo*. 219–231 (2003).
- Grusser, O. J., Pause, M. & Schreiter, U. Localization and responses of neurones in the parieto-insular vestibular cortex of awake monkeys (*Macaca fascicularis*). *J Physiol.* **430**(1), 537–57, <https://doi.org/10.1113/jphysiol.1990.sp018306> (1990).
- Grusser, O. J., Pause, M. & Schreiter, U. Vestibular neurones in the parieto-insular cortex of monkeys (*Macaca fascicularis*): visual and neck receptor responses. *J Physiol.* **430**(1), 559–83, <https://doi.org/10.1113/jphysiol.1990.sp018307> (1990).
- Guldin, W. & Grüsser, O. Is there a vestibular cortex? *Trends Neurosci.* **21**(6), 254–259 (1998).
- Eickhoff, S. B. *et al.* The human parietal operculum. I. Cytoarchitectonic mapping of subdivisions. *Cereb Cortex* **16**(2), 254–67, <https://doi.org/10.1093/cercor/bhi105> (2006).
- Eickhoff, S. B. *et al.* Identifying human parieto-insular vestibular cortex using fMRI and cytoarchitectonic mapping. *Hum Brain Mapp.* **27**(7), 611–21, <https://doi.org/10.1002/hbm.20205> (2006).
- zu Eulenburg, P. *et al.* Meta-analytical definition and functional connectivity of the human vestibular cortex. *Neuroimage.* **60**(1), 162–169, <https://doi.org/10.1016/j.neuroimage.2011.12.032> (2012).
- zu Eulenburg, P. *et al.* The human vestibular cortex. *ScienceOpen Posters*. (2020).
- Triarhou, L. C. The cytoarchitectonic map of Constantin von Economo and Georg N. Koskinas, in *Microstructural Parcellation of the Human Cerebral Cortex*, pp. 33–53 (Springer, 2013).
- Triarhou, L. C. A proposed number system for the 107 cortical areas of Economo and Koskinas, and Brodmann area correlations. *Stereotactic and Functional Neurosurgery.* **85**(5), 204–215, <https://doi.org/10.1159/000103259> (2007).
- Scholten, L. H. *et al.* An MRI von Economo–Koskinas atlas. *NeuroImage.* **170**, 249–256, <https://doi.org/10.1016/j.neuroimage.2016.12.069> (2018).
- Triarhou, L. C. The Economo–Koskinas atlas revisited: cytoarchitectonics and functional context. *Stereotactic and Functional Neurosurgery.* **85**(5), 195–203, <https://doi.org/10.1159/000103258> (2007).
- Raiser, T. M. *et al.* The human corticocortical vestibular network. *Neuroimage.* **223**, 117362, <https://doi.org/10.1016/j.neuroimage.2020.117362> (2020).
- Indovina, I. *et al.* Structural connectome and connectivity lateralization of the multimodal vestibular cortical network. *Neuroimage.* **222**, 117247, <https://doi.org/10.1016/j.neuroimage.2020.117247> (2020).
- Smith, J. L. *et al.* The “vestibular neuromatrix”: A proposed, expanded vestibular network from graph theory in post-concussive vestibular dysfunction. *Hum Brain Mapp.* (2021).
- Eckert, M. A. *et al.* At the heart of the ventral attention system: the right anterior insula. *Hum Brain Mapp.* **30**(8), 2530–2541 (2009).
- Rudebeck, P. H. *et al.* A role for primate subgenual cingulate cortex in sustaining autonomic arousal. *Proc Natl Acad Sci USA* **111**(14), 5391–6, <https://doi.org/10.1073/pnas.1317695111> (2014).
- Touroutoglou, A. *et al.* Dissociable large-scale networks anchored in the right anterior insula subserve affective experience and attention. *Neuroimage.* **60**(4), 1947–1958, <https://doi.org/10.1016/j.neuroimage.2012.02.012> (2012).
- Ben-Shabat, E. *et al.* The right supramarginal gyrus is important for proprioception in healthy and stroke-affected participants: a functional MRI study. *Front Neurol.* **6**, 248 (2015).
- Kheradmand, A., Lasker, A. & Zee, D. S. Transcranial magnetic stimulation (TMS) of the supramarginal gyrus: a window to perception of upright. *Cereb Cortex.* **25**(3), 765–71, <https://doi.org/10.1093/cercor/bht267> (2015).

22. Oane, I. *et al.* Cingulate cortex function and multi-modal connectivity mapped using intracranial stimulation. *NeuroImage*. **220**, 117059 (2020).
23. Potok, W. *et al.* The temporal involvement of the left supramarginal gyrus in planning functional grasps: A neuronavigated TMS study. *Cortex*. **111**, 16–34, <https://doi.org/10.1016/j.cortex.2018.10.010> (2019).
24. Britton, Z. & Arshad, Q. Vestibular and multi-sensory influences upon self-motion perception and the consequences for human behavior. *Front Neurol*. **10**, 63 (2019).
25. Baiano, M. *et al.* Anterior cingulate volumes in schizophrenia: a systematic review and a meta-analysis of MRI studies. *Schizophr Res*. **93**(1–3), 1–12, <https://doi.org/10.1016/j.schres.2007.02.012> (2007).
26. Bush, G., Luu, P. & Posner, M. I. Cognitive and emotional influences in anterior cingulate cortex. *Trends Cogn Sci*. **4**(6), 215–222, [https://doi.org/10.1016/s1364-6613\(00\)01483-2](https://doi.org/10.1016/s1364-6613(00)01483-2) (2000).
27. Hajek, T. *et al.* Reduced subgenual cingulate volumes in mood disorders: a meta-analysis. *J Psychiatry Neurosci*. **33**(2), 91–99 (2008).
28. Hatton, S. N. *et al.* Correlating anterior insula gray matter volume changes in young people with clinical and neurocognitive outcomes: an MRI study. *BMC Psychiatry*. **12**(1), 45, <https://doi.org/10.1186/1471-244X-12-45> (2012).
29. Silani, G. *et al.* Right supramarginal gyrus is crucial to overcome emotional egocentricity bias in social judgments. *J Neurosci*. **33**(39), 15466–15476 (2013).
30. Nakul, E., Bartolomei, F. & Lopez, C. Vestibular-Evoked Cerebral Potentials. *Front Neurol*. **12**, 674100, <https://doi.org/10.3389/fneur.2021.674100> (2021).
31. Lopez, C. The vestibular system: balancing more than just the body. *Curr Opin Neurol*. **29**(1), 74–83 (2016).
32. Mast, F. W. *et al.* Spatial cognition, body representation and affective processes: the role of vestibular information beyond ocular reflexes and control of posture. *Front Integr Neurosci*. **8**, 44, <https://doi.org/10.3389/fnint.2014.00044> (2014).
33. Brandt, T., Strupp, M. & Dieterich, M. Towards a concept of disorders of “higher vestibular function”. *Front Integr Neurosci*. **8**, 47 (2014).
34. Allen, J. W. *et al.* Altered Processing of Complex Visual Stimuli in Patients with Postconcussive Visual Motion Sensitivity. *AJNR Am J Neuroradiol*. **42**(5), 930–937, <https://doi.org/10.3174/ajnr.A7007> (2021).
35. Riccelli, R. *et al.* Altered insular and occipital responses to simulated vertical self-motion in patients with persistent postural-perceptual dizziness. *Front Neurol*. **8**, 529, <https://doi.org/10.3389/fneur.2017.00529> (2017).
36. Trofimova, A. *et al.* Alterations in topological organization of brain networks in subacute post-concussive central vestibular impairment using resting-state brain fMRI graph theory analysis, in *58th Annual Meeting of the American Society of Neuroradiology (ASNR)*, Las Vegas, Nevada (2020).
37. Trofimova, A. *et al.* Altered resting-state fMRI brain connectivity correlates with objective postural stability measures in patients with subacute post-concussion vestibular impairment, in *106th Scientific Assembly and Annual Meeting of the Radiological Society of North America (RSNA)*, Chicago, Illinois (2020).
38. Ponso, S. *et al.* Balancing body ownership: Visual capture of proprioception and affectivity during vestibular stimulation. *Neuropsychologia*. **117**, 311–321, <https://doi.org/10.1016/j.neuropsychologia.2018.06.020> (2018).
39. Preuss, N., Hasler, G. & Mast, F. W. Caloric vestibular stimulation modulates affective control and mood. *Brain Stimul*. **7**(1), 133–40, <https://doi.org/10.1016/j.brs.2013.09.003> (2014).
40. Passamonti, L. *et al.* Brain responses to virtual reality visual motion stimulation are affected by neurotic personality traits in patients with persistent postural-perceptual dizziness. *J Vestib Res*. **28**(5–6), 369–378, <https://doi.org/10.3233/VES-190653> (2018).
41. Staab, J. P. The influence of anxiety on ocular motor control and gaze. *Curr Opin Neurol*. **27**(1), 118–124, <https://doi.org/10.1097/WCO.000000000000055> (2014).
42. Van Essen, D. C. *et al.* The WU-Minn human connectome project: an overview. *Neuroimage*. **80**, 62–79, <https://doi.org/10.1016/j.neuroimage.2013.05.041> (2013).
43. Sudlow, C. *et al.* UK biobank: an open access resource for identifying the causes of a wide range of complex diseases of middle and old age. *PLoS medicine*. **12**(3), e1001779, <https://doi.org/10.1371/journal.pmed.1001779> (2015).
44. Casey, B. J. *et al.* The adolescent brain cognitive development (ABCD) study: imaging acquisition across 21 sites. *Dev Cogn Neurosci*. **32**, 43–54, <https://doi.org/10.1016/j.dcn.2018.03.001> (2018).
45. Siedhoff, H. R. *et al.* Perspectives on primary blast injury of the brain: translational insights into non-inertial low-intensity blast injury. *Front Neurol*. **12**, 818169 (2022).
46. Cifu, D.X. Clinical research findings from the long-term impact of military-relevant brain injury consortium—Chronic Effects of Neurotrauma Consortium (LIMBIC-CENC) 2013–2021. *Brain Injury*. **36**(5), 1–11, <https://doi.org/10.1080/02699052.2022.2033843>
47. O’Neil, M. E. *et al.* Associations among PTSD and postconcussive symptoms in the Long-Term Impact of Military-Relevant Brain Injury Consortium—Chronic Effects of Neurotrauma Consortium Prospective, longitudinal study cohort. *J Head Trauma Rehab*. **36**(6), E363–E372 (2021).
48. Ertl, M. & Boegle, R. Investigating the vestibular system using modern imaging techniques—A review on the available stimulation and imaging methods. *J Neurosci Methods*. **326**, 108363 (2019).
49. Ibitoye, R. T. *et al.* The human vestibular cortex: functional anatomy of OP2, its connectivity and the effect of vestibular disease. *Cereb Cortex*. <https://doi.org/10.1093/cercor/bhac085> (2022).
50. Eickhoff, S. B. *et al.* A new SPM toolbox for combining probabilistic cytoarchitectonic maps and functional imaging data. *Neuroimage*. **25**(4), 1325–35, <https://doi.org/10.1016/j.neuroimage.2004.12.034> (2005).
51. Eickhoff, S. B. *et al.* Testing anatomically specified hypotheses in functional imaging using cytoarchitectonic maps. *Neuroimage*. **32**(2), 570–82, <https://doi.org/10.1016/j.neuroimage.2006.04.204> (2006).
52. Eickhoff, S. B. *et al.* Assignment of functional activations to probabilistic cytoarchitectonic areas revisited. *Neuroimage*. **36**(3), 511–21, <https://doi.org/10.1016/j.neuroimage.2007.03.060> (2007).
53. Diedrichsen, J. *et al.* A probabilistic MR atlas of the human cerebellum. *Neuroimage*. **46**(1), 39–46, <https://doi.org/10.1016/j.neuroimage.2009.01.045> (2009).
54. Najdenovska, E., Yasser, A.-G. & Bach Cuadra, M. *In-vivo* probabilistic atlas of human thalamic nuclei based on diffusion weighted magnetic resonance imaging. *Zenodo*. <https://doi.org/10.5281/zenodo.1405484> (2018).
55. Neudorfer, C. *et al.* NSD Atlas of the Hypothalamic Region. *Zenodo*. <https://doi.org/10.5281/zenodo.1405484> (2020).
56. Najdenovska, E. *et al.* *In-vivo* probabilistic atlas of human thalamic nuclei based on diffusion-weighted magnetic resonance imaging. *Sci Data*. **5**(1), 1–11, <https://doi.org/10.1038/sdata.2018.270> (2018).
57. Neudorfer, C. *et al.* A high-resolution *in vivo* magnetic resonance imaging atlas of the human hypothalamic region. *Sci Data*. **7**(1), 1–14, <https://doi.org/10.1038/s41597-020-00644-6> (2020).
58. Singh, K., García-Gomar, M. G. & Bianciardi, M. Probabilistic atlas of the mesencephalic reticular formation, isthmus reticular formation, microcellular tegmental nucleus, ventral tegmental area nucleus complex, and caudal-rostral linear raphe nucleus complex in living humans from 7 Tesla magnetic resonance imaging. *Brain Conn*. **11**(8), 613–623, <https://doi.org/10.1089/brain.2020.0975> (2021).
59. Singh, K. *et al.* Probabilistic template of the lateral parabrachial nucleus, medial parabrachial nucleus, vestibular nuclei complex, and medullary visceromotor nuclei complex in living humans from 7 Tesla MRI. *Front Neurosci*. **13**, 1425, <https://doi.org/10.3389/fnins.2019.01425> (2020).
60. García-Gomar, M. G. *et al.* *In vivo* probabilistic structural atlas of the inferior and superior colliculi, medial and lateral geniculate nuclei and superior olivary complex in humans based on 7 tesla MRI. *Front Neurosci*. **13**, 764, <https://doi.org/10.3389/fnins.2019.00764> (2019).

61. Bianciardi, M. *et al.* A probabilistic template of human mesopontine tegmental nuclei from *in vivo* 7 T MRI. *Neuroimage*. **170**, 222–230, <https://doi.org/10.1016/j.neuroimage.2017.04.070> (2018).
62. Bianciardi, M. *et al.* Toward an *in vivo* neuroimaging template of human brainstem nuclei of the ascending arousal, autonomic, and motor systems. *Brain Conn*. **5**(10), 597–607, <https://doi.org/10.1089/brain.2015.0347> (2015).
63. García-Gomar, M. G. *et al.* Brainstem structural connectivity changes in isolated REM sleep behavior disorder by 7 Tesla MRI.
64. Bianciardi, M. *Brainstem Navigator v0.9*. NITRC. <https://doi.org/10.25790/bml0cm.96> (2021).
65. Fan, L. *et al.* The Human Brainnetome Atlas: a new brain atlas based on connectonal architecture. *Cereb Cortex*. **26**(8), 3508–26, <https://doi.org/10.1093/cercor/bhw157> (2016).
66. Jiang, T. Brainnetome: a new-ome to understand the brain and its disorders. *Neuroimage*. **80**, 263–272 (2013).
67. Wang, J. *et al.* Tractography-based parcellation of the human left inferior parietal lobule. *Neuroimage*. **63**(2), 641–652, <https://doi.org/10.1016/j.neuroimage.2012.07.045> (2012).
68. Zhang, Y. *et al.* Robust brain parcellation using sparse representation on resting-state fMRI. *Brain Structure Function*. **220**(6), 3565–3579 (2015).
69. Yang, Y. *et al.* Identifying functional subdivisions in the human brain using meta-analytic activation modeling-based parcellation. *Neuroimage*. **124**, 300–309 (2016).
70. Cox, R. W. AFNI: software for analysis and visualization of functional magnetic resonance neuroimages. *Comput Biomed Res*. **29**(3), 162–73, <https://doi.org/10.1006/cbmr.1996.0014> (1996).
71. Frank, S. M., Wirth, A. M. & Greenlee, M. W. Visual-vestibular processing in the human Sylvian fissure. *J Neurophysiol*. **116**(2), 263–71, <https://doi.org/10.1152/jn.00009.2016> (2016).
72. Frank, S. M. & Greenlee, M. W. The parieto-insular vestibular cortex in humans: more than a single area? *J Neurophysiol*. **120**(3), 1438–1450 (2018).
73. Smith, J. L. *et al.* *Eagle Atlas Compilation for Vestibular Research*. NITRC. <https://doi.org/10.25790/bml0cm.114> (2022).
74. Grefkes, C. *et al.* Human somatosensory area 2: observer-independent cytoarchitectonic mapping, interindividual variability, and population map. *Neuroimage*. **14**(3), 617–631, <https://doi.org/10.1006/nimg.2001.0858> (2001).
75. Geyer, S., Schleicher, A. & Zilles, K. Areas 3a, 3b, and 1 of human primary somatosensory cortex: 1. Microstructural organization and interindividual variability. *Neuroimage*. **10**(1), 63–83 (1999).
76. Geyer, S. *et al.* Areas 3a, 3b, and 1 of human primary somatosensory cortex: 2. Spatial normalization to standard anatomical space. *Neuroimage*. **11**(6), 684–696, <https://doi.org/10.1006/nimg.2000.0548> (2000).
77. Malikovic, A. *et al.* Cytoarchitectonic analysis of the human extrastriate cortex in the region of V5/MT+: a probabilistic, stereotaxic map of area hOc5. *Cereb Cortex*. **17**(3), 562–574, <https://doi.org/10.1093/cercor/bhj181> (2007).
78. Scheperjans, F. *et al.* Probabilistic maps, morphometry, and variability of cytoarchitectonic areas in the human superior parietal cortex. *Cereb Cortex*. **18**(9), 2141–2157, <https://doi.org/10.1093/cercor/bhm241> (2008).
79. Scheperjans, F. *et al.* Observer-independent cytoarchitectonic mapping of the human superior parietal cortex. *Cereb Cortex*. **18**(4), 846–867, <https://doi.org/10.1093/cercor/bhm116> (2008).
80. Caspers, S. *et al.* The human inferior parietal cortex: cytoarchitectonic parcellation and interindividual variability. *Neuroimage*. **33**(2), 430–448, <https://doi.org/10.1016/j.neuroimage.2006.06.054> (2006).
81. Caspers, S. *et al.* The human inferior parietal lobule in stereotaxic space. *Brain Struct Func*. **212**(6), 481–495, <https://doi.org/10.1007/s00429-008-0195-z> (2008).
82. Amunts, K. *et al.* Cytoarchitectonic mapping of the human amygdala, hippocampal region and entorhinal cortex: intersubject variability and probability maps. *Anat Embryol*. **210**(5), 343–352, <https://doi.org/10.1007/s00429-005-0025-5> (2005).
83. Kurth, F. *et al.* Cytoarchitecture and probabilistic maps of the human posterior insular cortex. *Cereb Cortex*. **20**(6), 1448–1461, <https://doi.org/10.1093/cercor/bhp208> (2010).
84. Palomero-Gallagher, N. *et al.* Cytology and receptor architecture of human anterior cingulate cortex. *J Comp Neurol*. **508**(6), 906–926, <https://doi.org/10.1002/cne.21684> (2008).
85. Henssen, A. *et al.* Cytoarchitecture and probability maps of the human medial orbitofrontal cortex. *Cortex*. **75**, 87–112, <https://doi.org/10.1016/j.cortex.2015.11.006> (2016).
86. Rottschy, C. *et al.* Ventral visual cortex in humans: cytoarchitectonic mapping of two extrastriate areas. *Hum Brain Mapp*. **28**(10), 1045–1059, <https://doi.org/10.1002/hbm.20348> (2007).
87. Kujovic, M. *et al.* Cytoarchitectonic mapping of the human dorsal extrastriate cortex. *Brain Struct Func*. **218**(1), 157–172, <https://doi.org/10.1007/s00429-012-0390-9> (2013).
88. Caspers, J. *et al.* Cytoarchitectonic analysis and probabilistic mapping of two extrastriate areas of the human posterior fusiform gyrus. *Brain Struct Func*. **218**(2), 511–526, <https://doi.org/10.1007/s00429-012-0411-8> (2013).
89. Lorenz, S. *et al.* Two new cytoarchitectonic areas on the human mid-fusiform gyrus. *Cereb Cortex*. **27**(1), 373–385, <https://doi.org/10.1093/cercor/bhv225> (2017).
90. Malikovic, A. *et al.* Cytoarchitecture of the human lateral occipital cortex: mapping of two extrastriate areas hOc4la and hOc4lp. *Brain Struct Func*. **221**(4), 1877–1897, <https://doi.org/10.1007/s00429-015-1009-8> (2016).
91. Behrens, T. E. *et al.* Non-invasive mapping of connections between human thalamus and cortex using diffusion imaging. *Nat Neurosci*. **6**(7), 750–757 (2003).
92. Behrens, T. E. *et al.* Characterization and propagation of uncertainty in diffusion-weighted MR imaging. *Magn Reson Med*. **50**(5), 1077–88, <https://doi.org/10.1002/mrm.10609> (2003).
93. Van Essen, D. C. & Ugurbil, K. The future of the human connectome. *Neuroimage*. **62**(2), 1299–1310, <https://doi.org/10.1016/j.neuroimage.2012.01.032> (2012).
94. Salimi-Khorshidi, G. *et al.* Automatic denoising of functional MRI data: combining independent component analysis and hierarchical fusion of classifiers. *Neuroimage*. **90**, 449–468, <https://doi.org/10.1016/j.neuroimage.2013.11.046> (2014).
95. Salkind, N. *Encyclopedia of Research Design*. <https://doi.org/10.4135/9781412961288> (2010).
96. Whitfield-Gabrieli, S. & Nieto-Castanon, A. Conn: a functional connectivity toolbox for correlated and anticorrelated brain networks. *Brain Connect*. **2**(3), 125–41, <https://doi.org/10.1089/brain.2012.0073> (2012).
97. Nieto-Castanon, A. *Handbook of functional connectivity Magnetic Resonance Imaging methods in CONN*. (Hilbert Press, 2020).
98. Smith, S. M. & Nichols, T. E. Threshold-free cluster enhancement: addressing problems of smoothing, threshold dependence and localisation in cluster inference. *Neuroimage*. **44**(1), 83–98, <https://doi.org/10.1016/j.neuroimage.2008.03.061> (2009).
99. Chumbley, J. *et al.* Topological FDR for neuroimaging. *Neuroimage*. **49**(4), 3057–64, <https://doi.org/10.1016/j.neuroimage.2009.10.090> (2010).
100. Bar-Joseph, Z., Gifford, D. K. & Jaakkola, T. S. Fast optimal leaf ordering for hierarchical clustering. *Bioinformatics*. **17**(Suppl 1), S22–9, https://doi.org/10.1093/bioinformatics/17.suppl_1.s22 (2001).
101. Gordon, E. M. *et al.* Generation and evaluation of a cortical area parcellation from resting-state correlations. *Cereb Cortex*. **26**(1), 288–303, <https://doi.org/10.1093/cercor/bhu239> (2016).
102. Risk, B. B. *et al.* Which multiband factor should you choose for your resting-state fMRI study? *NeuroImage*. **234**, 117965 (2021).
103. Risk, B. B., Kociuba, M. C. & Rowe, D. B. Impacts of simultaneous multislice acquisition on sensitivity and specificity in fMRI. *NeuroImage*. **172**, 538–553, <https://doi.org/10.1016/j.neuroimage.2018.01.078> (2018).

Acknowledgements

The present work was supported by NIH/NINDS grant R01NS119683 and a seed grant from the Emory University Department of Radiology and Imaging Sciences. The authors would also like to thank Drs. Iole Indovina and Peter zu Eulenburg for providing several ROI templates, including OP2 and PIC.

Data were provided in part by the Human Connectome Project, WU-Minn Consortium (Principal Investigators: David Van Essen and Kamil Ugurbil; 1U54MH091657) funded by the 16 NIH Institutes and Centers that support the NIH Blueprint for Neuroscience Research; and by the McDonnell Center for Systems Neuroscience at Washington University.

Author contributions

All authors contributed substantively to the work presented in this paper. J.W.A. and R.K.G. jointly conceived, designed, and supervised implementation of the study and provided clinical interpretation of the results. J.L.S. compiled the original source atlases, conducted the processing and quality assurance workflows for merging of the source atlases, and performed the technical validation using Human Connectome Project data. V.A., J.W.A. and R.K.G. supervised the analysis and edited the manuscript.

Competing interests

The authors declare no competing interests.

Additional information

Supplementary information The online version contains supplementary material available at <https://doi.org/10.1038/s41597-023-01938-1>.

Correspondence and requests for materials should be addressed to J.W.A.

Reprints and permissions information is available at www.nature.com/reprints.

Publisher's note Springer Nature remains neutral with regard to jurisdictional claims in published maps and institutional affiliations.



Open Access This article is licensed under a Creative Commons Attribution 4.0 International License, which permits use, sharing, adaptation, distribution and reproduction in any medium or format, as long as you give appropriate credit to the original author(s) and the source, provide a link to the Creative Commons license, and indicate if changes were made. The images or other third party material in this article are included in the article's Creative Commons license, unless indicated otherwise in a credit line to the material. If material is not included in the article's Creative Commons license and your intended use is not permitted by statutory regulation or exceeds the permitted use, you will need to obtain permission directly from the copyright holder. To view a copy of this license, visit <http://creativecommons.org/licenses/by/4.0/>.

© The Author(s) 2023